MATERIALS SCIENCE

Homo-layer flexible Bi_2Te_3-based films with high thermoelectric performance

Dasha Mao[1]†, Jianmin Yang[1,2]†, Meng Han[3]†, Xiege Huang[4], Jianrui Wang[1], Baohai Jia[1], Zhongbin Wang[1], Xiao Xu[1], Lin Xie[1,5], Yi Zhou[1,6]*, Guodong Li[4], Ghim Wei Ho[6], Jiaqing He[1,7]*

Here, we demonstrate unconventional scalable and sustainable manufacturing of flexible n-type Bi_2Te_3 films via physical vapor deposition and homo-layer fusion engineering. The achieved ultrahigh power factor of up to 30.0 microwatts per centimeter per square kelvin and ultralow lattice thermal conductivity of 0.38 watts per meter per kelvin at room temperature are attributed to the synergy of modulated modest carrier concentration and weighted mobility in homo-layer films. These results bring forth a maximum output power density of 300 watts per square meter at a temperature gradient of 60 kelvin and a normalized cooling factor of 0.6, which is sufficient to sustain consumer electronics with large-area manufacturing of up to 120 square centimeters. Our developed homo-layer deposition with industry compatibility and scalability potentials highlights a facile yet cost-effective strategy, not only for structure-property relation manipulation in inorganic semiconductors but also for solid-state electronic fabrication for heat harvesting and management frontiers.

INTRODUCTION

Thermoelectricity (TE) is capable of direct energy conversion between heat and electricity, promising low-grade heat harvesting (<100°C) and solid-state cooling toward the transition of sustainable electronics (*1*). The energy conversion efficiency (or cooling coefficient of performance, η) of TEs is normally determined by the dimensionless figure of merit, $ZT = S^2\sigma T/\kappa_{tot}$, where S, σ, κ_{tot}, and T represent the Seebeck coefficient, electrical conductivity, total thermal conductivity, and absolute temperature, respectively. While the ZT value and power factor ($PF = S^2\sigma$) are limited by the intercoupled carrier transport and electronic band structure (e.g., $S \propto n^{-2/3}$, $\sigma \propto n$; $S \propto m^*$, $\sigma \propto 1/m^*$; where n is the carrier concentration and m^* is the effective mass), especially for degenerate TEs with a heavy doping concentration (*2*, *3*). Also, in terms of nonplanar/curved heat harvesting or cooling, superior TEs with bendability are required to minimize heat loss for a desirable temperature difference and efficiency (i.e., $\eta \propto \Delta T$). Recently, turning bulk ingots into thin films through physical vapor deposition (PVD) (*4*, *5*), mechanical exfoliation (*6*), and inherent ductility was demonstrated (*7*, *8*), which brings forth a ZT of >1.0 in p-type bismuth telluride (Bi_2Te_3) with scalability and flexibility (*9*–*12*). However, as device deployment necessitates a performance match between p- and n-type legs to maximize the overall ZT, and thus, n-type TEs with high PF, flexibility, and scalability are urged to be developed, especially for room temperature applications.

To date, bulk Bi_2Te_3 polycrystalline undergoes a composite synthesis process that typically encompasses melting, ball milling, hot pressing, and spark plasma sintering (*13*–*16*), aiming to introduce a myriad of structural defects for enhanced performance. Conversely, the synthesis procedure of thin films is constrained by the physical thickness and substrate compatibility, where singular deposition methodologies with performance enhancement are largely reliant on postdeposition annealing treatment. Despite tremendous efforts such as dopant and texture manipulations in a PVD process (*17*, *18*), and nanobinders prepared by wet chemical method in a screen-printed process (*1*), surpassing a power factor threshold of 20 μW cm^{-1} K^{-2} at room temperature in n-type Bi_2Te_3 thin films through singular synthesis routes remains an elusive goal. In addition, while ultrahigh performance TE films can be obtained through exfoliation from single crystals (*6*), the limited scalability (<5 cm^2) hinders practical applications. These conventional methods also pose challenges in fine-tuning key parameters such as the Seebeck coefficient, electrical conductivity, or scalability, as summarized in the realm of n-type Bi_2Te_3 thin films (table S1) (*1*, *6*, *17*–*26*). Consequently, state-of-the-art fabrication methodologies to advance n-type TE films for on-demand implications include (i) modulation of n and weighted mobility for PF maximization; (ii) sustaining high PF and ZT with superior flexibility; and (iii) scalable and sustainable manufacturing with cost-effectiveness.

In this work, we used a unique approach that harnesses the synergy of magnetron sputtering (MS) and vacuum thermal evaporation (VTE) to fabricate a homo-layer–fused $Bi_2Te_{2.85}Se_{0.15}$ film (i.e., VTE layer, 500 nm; MS layer, 500 nm; marked as VTE@MS-BTS). Our comparative analysis differs from traditional single-method deposition (MS-BTS or VTE-BTS films), and we deposited a series of VTE@*t*%MS-BTS films [*t*% = MS-layer thickness/(VTE + MS) × 100%, the total thickness fixed at 1 μm] with precisely adjusted MS-layer proportions. For instance, the films of *t*% = 17% (830 to 170 nm), 38% (620 to 380 nm), 64% (360 to 640 nm), and 72% (280 to 720 nm). Here, the modulation of n and mobility (μ) with variable thickness proportions (*t*%) through homo-layer fusion is an analogy of element doping (stoichiometric ratio) in thermoelectrics. Specifically, the developed VTE@MS-BTS synergistically modulates the Seebeck coefficient, electrical conductivity,

[1]Department of Physics, State Key Laboratory of Quantum Functional Materials, and Guangdong Basic Research Center of Excellence for Quantum Science, Southern University of Science and Technology, Shenzhen 518055, China. [2]Department of Materials Science and Engineering, National University of Singapore, Singapore 117575, Singapore. [3]Shenzhen Institute of Advanced Electronic Materials, Shenzhen Institute of Advanced Technology, Chinese Academy of Sciences, Shenzhen 518055, China. [4]Hubei Key Laboratory of Theory and Application of Advanced Materials Mechanics, School of Physics and Mechanics, Wuhan University of Technology, Wuhan 430070, China. [5]School of Physical Sciences, Great Bay University, Dongguan 523000, China. [6]Department of Electrical and Computer Engineering, National University of Singapore, Singapore 117581, Singapore. [7]Guangdong Provincial Key Laboratory of Advanced Thermoelectric Materials and Device Physics, and Shenzhen Key Laboratory of Thermoelectric Materials, Southern University of Science and Technology, Shenzhen 518055, China.
*Corresponding author. Email: zhouyi@u.nus.edu (Y.Z.); hejq@sustech.edu.cn (J.H.)
†These authors contributed equally to this work.

thermal conductivity, and mechanical flexibility of the film. Ultimately, an ultrahigh power factor of up to 30.0 μW cm^{-1} K^{-2} and a ZT value of 1.0 at room temperature are achieved, and the bendability is also enhanced because of induced microstructural defects. Moreover, integrating this advanced film into planar device configurations demonstrates a high output performance for competitive power generation and cooling. Consequently, our work provides a pivotal framework for the understanding and manipulation of structure-property relations in TE thin films, thereby contributing to the advancement of scalable and flexible inorganic semiconductors.

RESULTS

Traditionally, the fabrication of TE films lies in individual synthesis processes, and thus, the global manipulation of structure-property relations and synergies targeting superior TE performance with scalability potential is limited. In contrast, our proposed homo-layer annealing treatment harnesses the merits of MS (texturization, orientation alignment, and high *n*) and VTE (high porosity, internal strain, and μ) for controllable film deposition (fig. S1; see Materials and Methods for details). This unconventional approach successfully decouples electrical and thermal transport properties while maintaining outstanding flexibility and scalability (Fig. 1A). The resultant film fused homogeneously yields a concurrent increment in both Seebeck coefficient and electrical conductivity, bringing forth a remarkable PF of 30.0 μW cm^{-1} K^{-2} at ambient temperature. Our film can also be manufactured in a large area of up to 120 cm^2 (fig. S1C), which outperforms that of other materials synthesized via conventional physical and chemical methodologies (Fig. 1B and table S1) (*1*, *6*, *17*–*26*). Furthermore, the flexible n-type films assembled with previously reported p-type TEs (*27*) demonstrate an impressive maximum output power density of 300 W m^{-2} at a temperature difference of 60 K. These results are competitive in the realm of chalcogenide and organic flexible TE generators (f-TEGs) for near room temperature applications (Fig. 1C and table S2) (*17*, *20*, *25*, *28*–*41*).

Structure characterization and underlying mechanism

Micro/nanostructures are pivotal for the manipulation of electrical and thermal transport properties in TEs, and particularly, the grain/texture evolution and homo-layer fusion under thermal annealing were investigated (see Materials and Methods for details). The tape peeling tests (fig. S2) demonstrated strong adhesion between the MS-first deposition layer and polyimide (PI) substrate due to enhanced

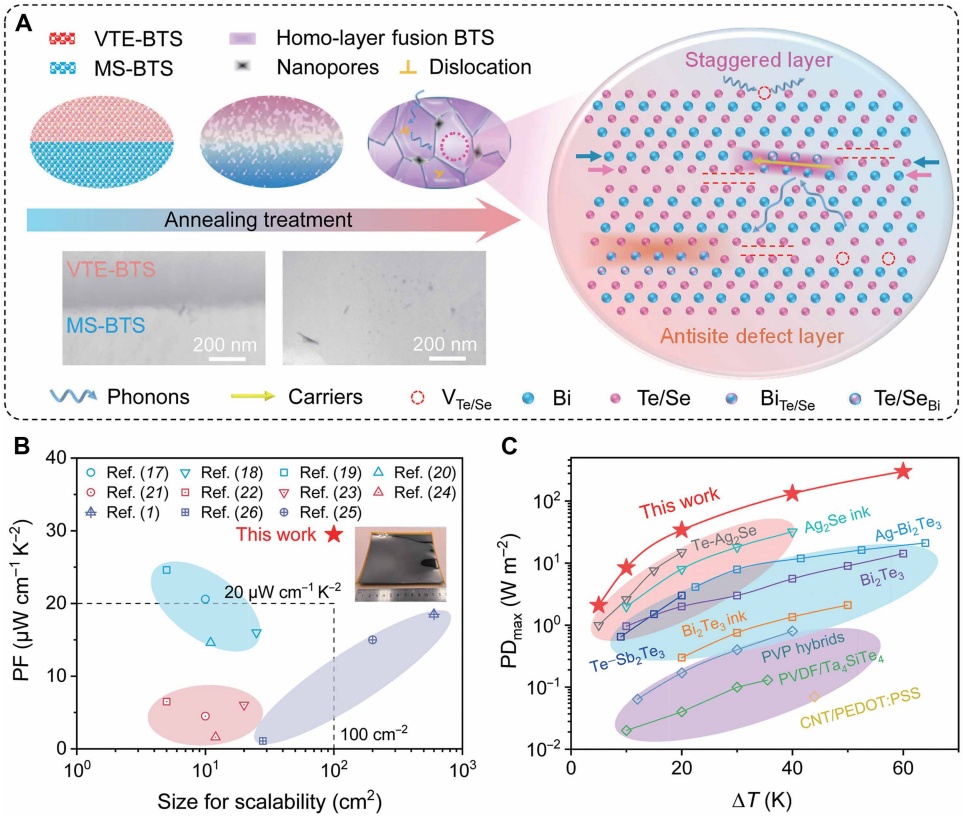

Fig. 1. Homo-layer fusion–derived electron-phonon decoupling to enhance TE performance and output power density. (**A**) Schematic diagram of homo-layer fusion and corresponding microstructure, with detailed insets highlighting the carrier and phonon scattering mechanisms in the VTE@MS-BTS film and the cross-section SEM images before and after annealing treatments. (**B**) State-of-the-art power factors at 300 K for n-type flexible Bi_2Te_3-based films prepared via PVD methods (MS, light blue region; VTE, light red region) and chemical methods (light purple region). For detailed data, refer to table S1. (**C**) Maximum output power density (PD_{max}) as a function of temperature difference (Δ*T*) and previously reported works. The light red, light blue, and light purple region represent f-TEGs with TE legs fabricated using Ag_2Se-based (*28*–*31*), Bi_2Te_3-based (*17*, *20*, *25*, *32*), and organic thin films (*39*–*41*), respectively. For detailed data, refer to table S2. PVP, polyvinylpyrrolidone; PVDF, polyvinylidene difluoride; CNT, carbon nanotube; PEDOT:PSS, poly(3,4-ethylenedioxythiophene):poly(styrene sulfonate).

mechanical interlocking (*42*), justifying the focus on VTE@MS-BTS over MS@VTE-BTS structures. Also, scanning electron microscopy (SEM; fig. S3) analysis revealed pore-free dense textures in MS-BTS annealed at 698 K, contrasting sharply with VTE-BTS counterparts and exhibiting substantial nanoscale porosity. Notably, the nanopores on the VTE@MS-BTS film surface were gradually enlarged and optimally tailored through annealing treatment (fig. S4). The combined application of ion-milled surface thinning and focused ion beam (FIB) techniques provided a comprehensive and direct view of the internal microstructure of the VTE@MS-BTS film (fig. S5, A to C). This analysis demonstrated that the two layers had coalesced into a uniform entity after annealing, with observed nanoscale pores predominantly confined to the grain boundaries. The energy dispersive spectroscopy (EDS) further validated homogeneous element distribution without secondary phases (fig. S5, D to F). This pore evolution during the homo-layer fusion is mainly ascribed to the VTE-deposited layer, and the porous texture serves as a heat and stress buffer with reduced film density (table S3) and mechanical strain, thereby lowering κ_{tot} (*43*–*46*). In addition, systematic x-ray diffraction (XRD) studies (Fig. 2A) further revealed that the (*00l*) texture intensity scales directly with the relative thickness of the MS layer. The VTE-BTS film exhibits indiscernible (*00l*) texture, whereas the MS- and VTE@MS-BTS films show pronounced (*00l*) texture, which was further visually confirmed by electron backscatter diffraction (EBSD) analysis (fig. S6). The (*00l*) orientation factor stabilizes at 0.22 to 0.27 (Fig. 2B) when the MS layer constitutes a total thickness of

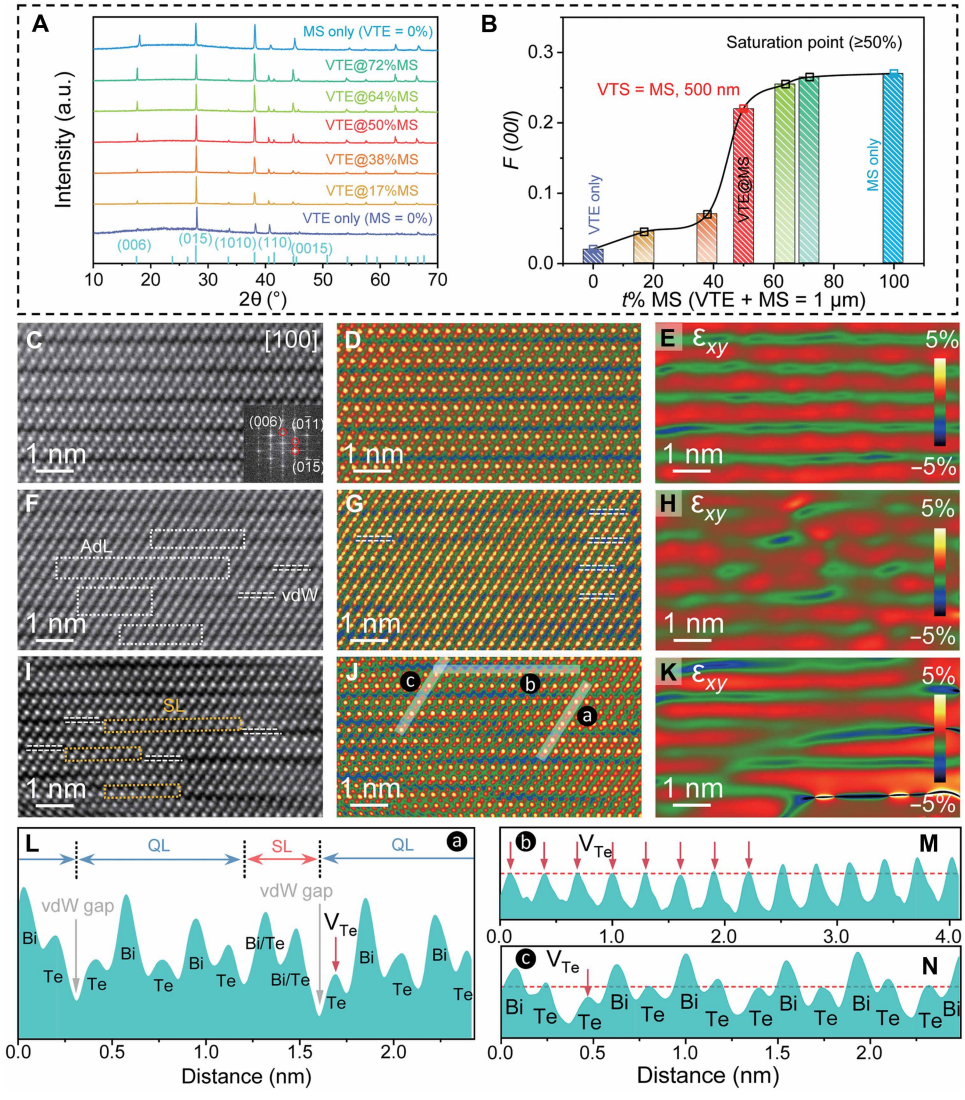

Fig. 2. Microstructure and characterization of BTS films. (**A**) XRD spectra of BTS thin films with the texturization modulated by variable MS-thickness ratios (all samples annealing under 698 K). JCPDS (Joint Committee on Powder Diffraction Standards) card is no. 51-0643. (**B**) Corresponding to (*00l*) orientation factors for as-prepared BTS films, highlighting the templating effect of the MS-BTS sublayer on crystallographic alignment. (**C** and **D**) High-angle annular dark-field (HAADF)–STEM image demonstrating quintuple-layer (QL) structure in the VTE-BTS film and (**E**) corresponding strain mapping with uniform stress distribution across lattice fringes. (**F** and **G**) HAADF-STEM image of the MS-BTS film and (**H**) corresponding strain mapping with nearly collapsed vdW gaps due to Bi-Te antisite defect layers (AdLs). (**I** and **J**) HAADF-STEM image showing notable staggered layers (SLs) in the VTE@MS-BTS film and (**K**) corresponding strain mapping with strain redistribution around SLs. (**L** to **N**) Intensity profiles of atomic columns across the vdW gap and V_{Te}, corresponding to the white semitransparent line in (J). a.u., arbitrary units.

≥50%, suggesting dominated texturization from the MS layer in VTE@*t*%MS-BTS films. The thickness modulation underpins these structural effects alongside step profiler measurement (fig. S7, A to F) and atomic force microscopy confirmation of ultralow surface roughness (~12 nm) (fig. S7, G and H), validating controlled deposition of 500-nm-thick MS and VTE layers with exemplified thickness tunability of 1 μm homo-layer after annealing.

To thoroughly investigate the atomic structural characteristics of the fused homo-layer composite BTS film, the cross-sectional lamellae of MS-only, VTE-only, and VTE@MS-BTS films were characterized via scanning transmission electron microscopy (STEM). High-resolution STEM images unraveled distinct microstructural features across the three samples (Fig. 2, C to K). For instance, the VTE-only film (0%) retains a quintuple-layer (QL) structure with pronounced van der Waals (vdW) gaps and negligible dislocations (Fig. 2, C to E), consistent with its low-energy growth mechanism (*6*). By contrast, the MS-only film (100%) exhibits nearly collapsed vdW gaps (Fig. 2, F to H) due to interlayer attraction induced by Bi-Te antisite defects, as corroborated by geometric phase analysis (Fig. 2H) and prior reports on plastically deformed Bi_2Te_3-based systems (*7*), where high-energy processes promote antisite defect layers (AdLs). The homo-layer fusion VTE@MS-BTS film (50%), however, reveals various defect structures where staggered layer (SL) defects dominate, with only minor antisite defects (Fig. 2, I to K). This hybrid microstructure arises from the interplay between the high-energy sputtered MS sublayer and the subsequent VTE-mediated defect reorganization. To further validate the universality of these structural and compositional features, a large-area STEM observation (16 nm by 16 nm; fig. S8) was imaged. This large-scale analysis not only confirms the consistent presence of collapsed vdW gaps in the MS-BTS film and SL defects in the VTE@MS-BTS film but also reveals Te vacancies [V_{Te}, marked with white arrows in fig. S8 (D and F)] across both samples. Also, these results were confirmed by atomic intensity line profile (Fig. 2, L to N) acquired from the semitransparent line regions in Fig. 2J. We attribute the higher n (~4.6×10^{20} cm^{-3}) in the MS-BTS film to the synergistic effects of high-energy sputtering and postannealing, where the former introduces antisite defects with a donor-like effect (*47*–*50*) and the latter promotes V_{Te} formation.

Electrical transport characterization

To understand how homo-layer annealing modulates electrical performance and transport characteristics toward a high PF, we evaluated the TE properties of MS- and VTE-BTS thin films separately (fig. S9; see Materials and Methods for details). Both films exhibited a maximum PF (8.0 μW cm^{-1} K^{-2} for the MS-BTS film and 8.5 μW cm^{-1} K^{-2} for the VTE-BTS film) at T_{ann} of 698 K. In comparison, the PF peaked at 30.0 μW cm^{-1} K^{-2} for VTE@MS-BTS thin films under an optimal T_{ann} of 698 K (fig. S10), owing to a delicate balance between the increment of S and σ (fig. S10D). The reproducibility and robustness of our results were confirmed by cross-institutional measurements (fig. S11) combined with the uncertainty analysis (table S4). These findings were examined further by thermoelectric characterization of three BTS thin films (Fig. 3, A to C). The VTE- and MS-BTS films presented distinct electrical properties. For instance, the former represented an elevated S with diminished σ, whereas the latter exceled in σ yet suffered from a reduced S (fig. S9, A and B). This trade-off in TE parameters for each film resulted in a relatively low PF of less than 8.5 μW cm^{-1} K^{-2} (Fig. 3C). In contrast, the proposed VTE@MS-BTS film harnesses the merits of both MS- and VTE-deposited films, and thus, a high S comparable with that of VTE-BTS coupled with the superior σ of MS-BTS is achieved.

Furthermore, to systematically examine the mobility doping decoupling in the homo-layer–fused process, electrical transport performance was evaluated across BTS films with variable MS proportions (*t*%). As plotted in fig. S12, the S exhibits an inverse relationship with σ as the MS layer thickness increases. In terms of the carrier transport properties (fig. S13), the n arises from V_{Te} in the MS layer would introduce additional electrons, with progressive modulation achieved by increasing the thickness proportion of MS layer (i.e., 3.4×10^{19} cm^{-3} at 17%, 4.6×10^{19} cm^{-3} at 38%, 7.4×10^{19} cm^{-3} at 50%, 1.2×10^{20} cm^{-3} at 64%, and 1.8×10^{20} cm^{-3} at 72%). The broad n range enabled definitive Pisarenko plot construction (Fig. 3, D to F; see Materials and Methods for details), which offers conclusive evidence for mobility doping decoupling while simultaneously revealing the characteristic inverse correlation between n and S. It is observed that while the MS layer introduces substantial carriers, the homo-layer fusion process concurrently enhances the m*. The m* of VTS@MS-BTS films is greater than that of VTE-BTS films, as well as other reported n-type Bi_2Te_3-based thin films (Fig. 3D) (*16*, *17*, *20*, *51*–*53*). This compensation mechanism preserves high S despite increased n. Notably, the stabilization of m* allows n to dominate the electrical transport, unraveling the accelerated decline in S. Also, Fig. 3E demonstrates that the m* enhancement does not compromise μ in low defect density (VTE-BTS and VTE@MS-BTS). This resilience originates from the (*00l*)-textured growth preference in MS-derived layers, a feature preserved through homo-layer fusion and quantitatively verified by XRD and EBSD analysis (Fig. 2, A and B, and fig. S6). Increasing MS content progressively strengthens this texture alignment until reaching parity between VTE@MS- and pure MS-BTS samples. Beyond this texture saturation point, continued MS proportion escalation induces excessive carrier-carrier scattering owing to increased n, bringing forth a decrease in μ. By balancing these competing mechanisms, we identify an optimal VTE-to-MS thickness ratio (50%, i.e., VTE@MS-BTS) that maximizes n while maintaining a favorable μ (83 cm^2 V^{-1} s^{-1}). Ultimately, the PF of VTE@MS-BTS films is substantially enhanced because of the optimized n, compared to that of MS- and VTE-BTS films (Fig. 3F).

Moreover, to physically justify the mechanism of the change in m*, we established atomic models based on the identified defect configurations (as characterized through detailed STEM analysis) and performed density functional theory (DFT) calculations (fig. S14; see Materials and Methods for details). The calculated band structures enabled the extraction of total density of states (DOS), which agrees well with the single parabolic band (SPB) results derived from experimental data (Fig. 3, D and G to I). Specifically, SL, AdL, and V_{Te} defects introduce localized perturbations in the crystal lattice, which flatten the energy dispersion near the conduction band minimum (CBM). This is evidenced by the increased slope of the DOS near the CBM in DFT calculations (Fig. 3G), suggesting reduced band curvatures. Consequently, the m* calculated from the band curvature in the Brillouin zone (K_x, K_y, and K_z) increases as these defects are introduced in the Bi_2Te_3-based system (Fig. 3H). These results are consistent with the SPB calculation from experiment data [m* increased from 1.2 m_0 (VTE only) to approximately 2.0 m_0 (VTE@MS-BTS); Fig. 3D]. However, the defect density exceeds a critical threshold when MS-layer proportions (*t*%) continuously increase, stabilizing band distortions and halting further

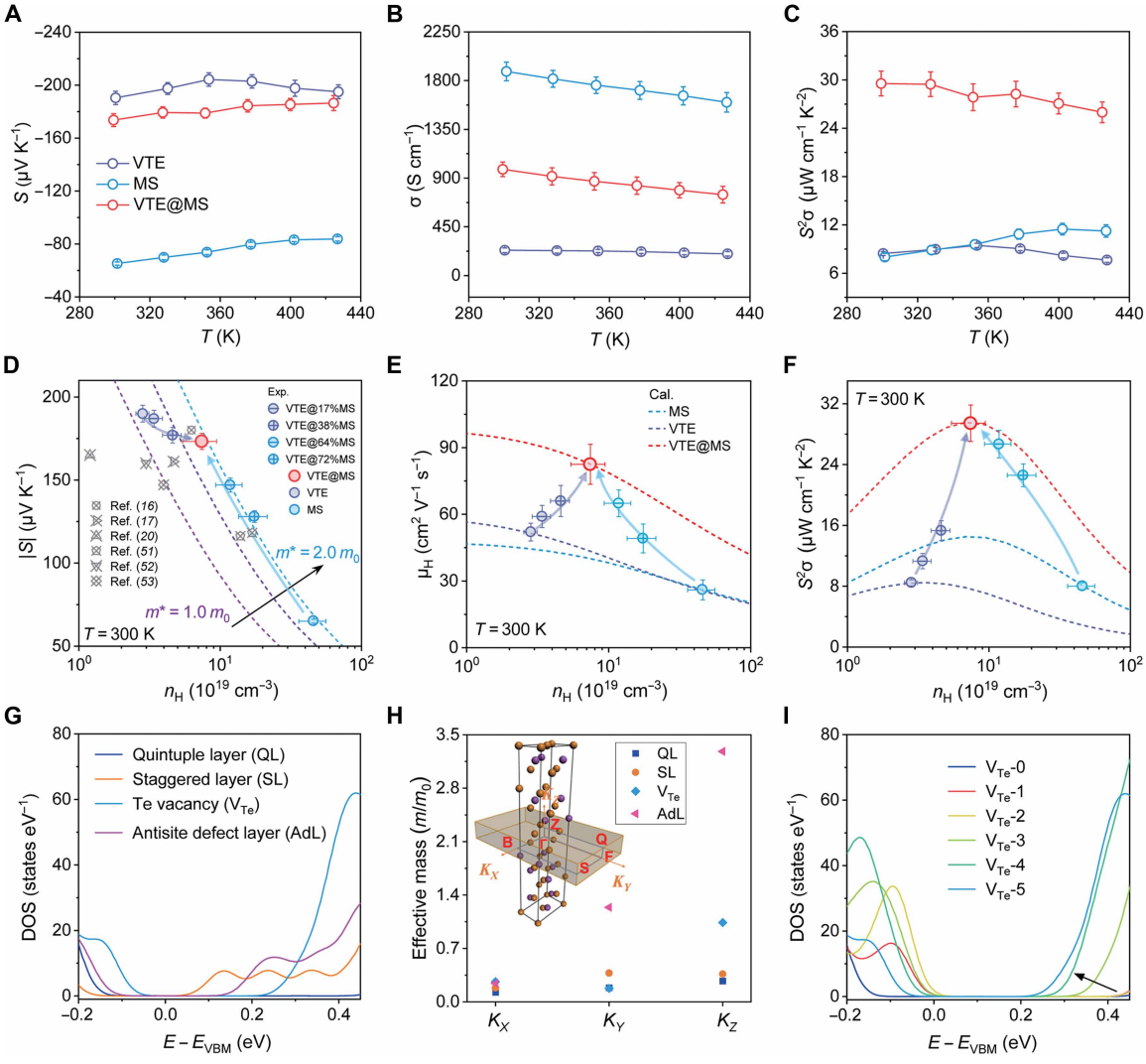

Fig. 3. Multiscale electronic properties and band structure of BTS films. Temperature dependence of (**A**) Seebeck coefficient, (**B**) electrical conductivity, and (**C**) power factor of BTS thin films. Pisarenko plots for (**D**) absolute Seebeck coefficient, (**E**) mobility, and (**F**) power factor of BTS thin films as a function of carrier concentration derived from SPB model at 300 K. (**G**) Calculated total DOS of Bi_2Te_3 with distinct defect configurations (SL, AdL, and V_{Te}). (**H**) Calculated effective mass (m^*) values corresponding to (G). (**I**) Calculated total DOS of Bi_2Te_3 with distinct V_{Te} concentrations.

increases in m^*. To elucidate this phenomenon, we constructed a series of models [designated as V_{Te}-0 (pristine) to V_{Te}-5] to simulate increasing Te vacancy incorporation. As shown in the DOS calculations (Fig. 3I), for the low Te vacancy concentrations (V_{Te}-0 → V_{Te}-3), a sharp increase in DOS slope near the CBM indicates notable band flattening and an elevated m^*. Beyond a critical defect threshold (V_{Te}-3 → V_{Te}-5), further vacancy introduction minimally alters the DOS slope, suggesting stabilized band curvature and saturation of m^*. This saturation occurs because localized lattice distortions reach a stable configuration, limiting additional band curvature changes. The behavior rationalizes the m^* plateau in MS-rich samples (VTE@MS to MS only), where defect densities exceed the threshold. Our analysis reveals that the saturation of m^* occurs when defects beyond a critical concentration that supported by experimental observations and first-principles calculations. This defect-driven band flattening and saturation at high defect density explain the nonmonotonic trend in m^*.

In addition, six thermoelectric cycling tests (fig. S15) and four cross-batch reproducibility (fig. S16) of VTE@MS-BTS thin film within the temperature range from 300 to 423 K revealed exceptional stability and durability of homo-layer fused film. Also, XRD characterization on the samples before and after transport measurements (fig. S17) demonstrated that the peak positions and relative intensities remain unchanged, indicating no detectable structural degradation or phase transition during the measurement process. Nanoindentation analyses (fig. S18) further confirmed mechanical resilience, showing minimal deviations (<15%) in elastic modulus and microhardness after 6-cycle TE measurement, which demonstrated the material's structural integrity and operational longevity under operational conditions.

Thermal transport characterization

Aside from the achieved high PF, the primary defect scattering of microstructures could modulate the thermal transport properties of

the films. Figure 4A presented the temperature-dependent in-plane total thermal conductivity (κ_{tot}) of BTS films by transient photo-electro-thermal (TPET) technique (fig. S19; see Materials and Methods for details), and the room temperature κ_{tot} was reduced from 1.76 W m^{-1} K^{-1} (MS-BTS film) to 0.86 W m^{-1} K^{-1} (VTE@MS-BTS film) (fig. S20 and table S3). Here, the decrease in κ_{tot} is primarily attributed to two components, the charge carrier thermal conductivity (κ_e) and the lattice thermal conductivity (κ_l). Specifically, κ_e was calculated by using the Wiedemann-Franz law (*54*, *55*), i.e., $\kappa_e = L_0\sigma T$, where L_0 is the Lorenz number estimated by the previously discussed SPB model. Given that the value of L_0 remains relatively invariant at temperatures below 423 K, three distinct constants were used to perform the calculation across the entire temperature range (300 to 423 K) for corresponding samples (table S3). Notably, the MS-BTS film results in an exceptionally elevated κ_e due to a high σ (Fig. 3B and figs. S9B and S13). Conversely, the VTE-BTS sample presents an opposing characteristic, as characterized by a reduced κ_{tot} and, subsequently, a lower κ_e (Fig. 4B). Also, the combined value of κ_l and bipolar thermal conductivity (κ_{bip}) was derived by $\kappa_{tot} - \kappa_e$, as plotted in Fig. 4C. Noticeably, at room temperature, the bipolar effect is extremely weak and negligible (*56*), so $\kappa_{tot} - \kappa_e$ is regarded as the κ_l. These results indicate that the κ_l of MS-BTS film is smaller than that of VTE-BTS film, while VTE@MS-BTS film exhibits the lowest κ_l of 0.38 W m^{-1} K^{-1}. To further elucidate the contribution of phonon scattering to the reduced κ_l, we conducted a meticulous calculation of thermal transport properties using the Debye-Callaway model (Fig. 4D; see Materials and Methods for details). The frequency-dependent spectral lattice thermal conductivity (κ_s) can be given below (*54*, *57*–*61*)

$$\kappa_l = \int_0^{\omega_D} \kappa_s(\omega)d\omega \quad (1)$$

where ω_D is the Debye frequency ($\omega_D = \theta_D/T$). The integrand item κ_s can be further described as follows

$$\kappa_s = \frac{k_B}{2\pi^2 v_a}\left(\frac{k_B T}{a\hbar}\right)^3 \frac{x^4 e^x}{\tau_C^{-1}(e^x-1)^2} \quad (2)$$

here, k_B, $\hbar$, v_a, θ_D are the Boltzmann constant, reduced Plank constant, average sound velocity, and Debye temperature, respectively. $x = \hbar\omega/k_B T$ is the simplified phonon frequency, ω is the phonon frequency. The total relaxation time τ_C is determined by Matthiessen's rule with the inclusion of the scattering contributions of various mechanisms: Umklapp process (τ_U), grain boundaries (τ_{GB}), point defects (τ_{PD}), dislocation scattering (τ_D), and stacking faults (SLs and AdLs; τ_{SF}). The detailed calculation can be found in Materials and Methods and table S5. The calculated results demonstrate that the point defects can lead to a rapid decrease in κ_l by scattering the high-frequency phonons. This also explains why the MS-BTS film with a high *n* of point defects exhibits a lower κ_l near room temperature compared to that of VTE-BTS film. In addition, the high *n* effectively suppresses

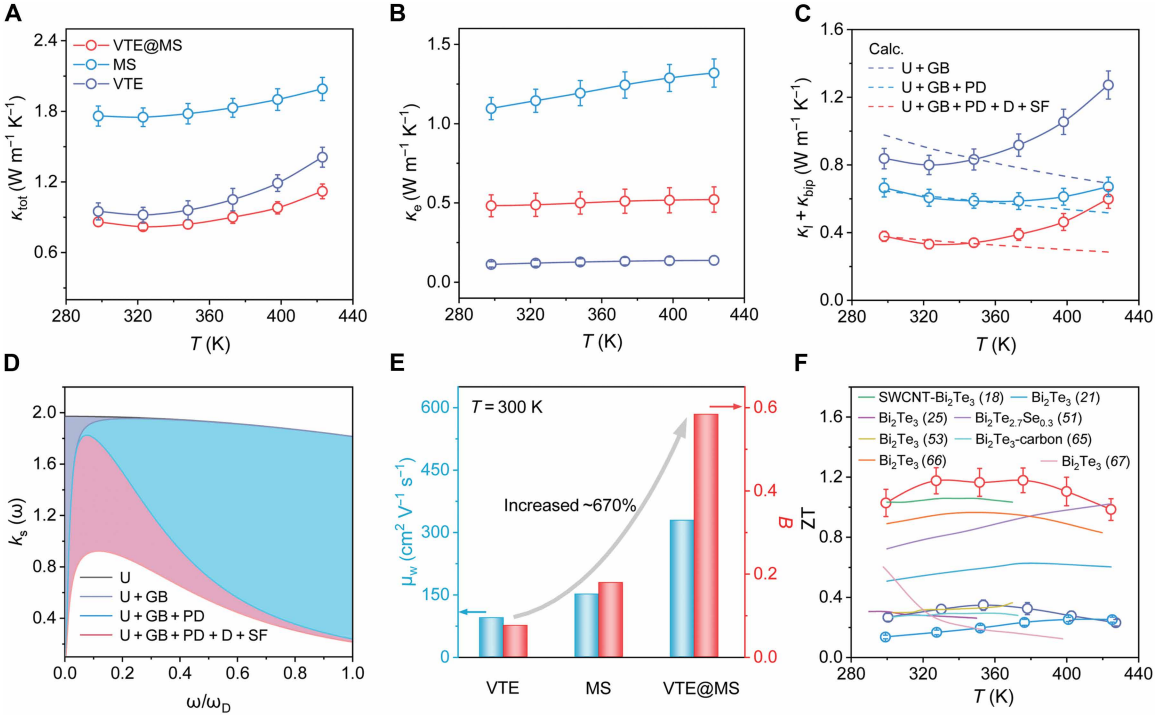

Fig. 4. Thermal transport properties and ZT values. Temperature dependence of (**A**) total thermal conductivities (κ_{tot}), (**B**) electrical thermal conductivities (κ_e), and (**C**) the sum of lattice thermal conductivities (κ_l) and bipolar thermal conductivities (κ_{bip}). (**D**) Frequency-dependent spectral lattice thermal conductivities (κ_s) calculated by the Debye-Callaway model at room temperature. U refers to the Umklapp process, GB refers to grain boundary scattering, PD refers to the point defect scattering without units, D refers to the dislocation scattering, and SF refers to the SL and AdL scattering. (**E**) Weighted mobility (μ_w) and quality factor (*B*) of BTS thin films at room temperature. (**F**) Temperature dependence of figure of merit (ZT) for BTS thin films. Solid lines represent in-plane ZT values for n-type Bi_2Te_3-based thin films reported in the literature.

the bipolar effect owing to increased collision and recombination probabilities between electrons and holes (*62*), leading to a comparable κ_l for the MS- and VTE@MS-BTS sample at a high temperature. Furthermore, the high-density SLs, AdLs, and dislocations introduced by homo-layer fusion primarily scatter mid-to-low–frequency phonons. Grain boundaries and the uniform distribution of nanopores around the grain boundaries are more sensitive to low-frequency phonons (*46*, *54*). Therefore, these defects synergistically contribute to creating full-scale phonon scattering centers, resulting in an extremely low κ_l in VTE@MS-BTS thin films (Fig. 4C).

To comprehensively assess the overall electron-phonon synergy of TE materials, we used the weighted mobility (μ_w) and quality factor (B) to evaluate the electronic qualities and ZT of the TE films (*63*). The calculation formulae are given as follows (*64*)

$$\mu_w = \frac{331}{\rho}\left(\frac{T}{300}\right)^{-1.5} \left\{\frac{\exp\left[\frac{|S|}{k_B/e} - 2\right]}{1+\exp\left[-5\left(\frac{|S|}{k_B/e} - 1\right)\right]} + \frac{\frac{3}{\pi^2}\frac{|S|}{k_B/e}}{1+\exp\left[5\left(\frac{|S|}{k_B/e} - 1\right)\right]}\right\} \quad (3)$$

where ρ is the electrical resistivity, $k_B/e = 86.3\ \mu V\ K^{-1}$, and

$$B = 4.33 \times 10^{-10}\frac{\mu_w T^{2.5}}{\kappa_l} \quad (4)$$

The calculated μ_w and B of as-synthesized TE films are plotted in Fig. 4E, where the VTE@MS-BTS film demonstrates the highest μ_w of up to 329 $cm^2\ V^{-1}\ s^{-1}$. Because of its high μ_w and low κ_l, the quality factor B of this film reaches 0.58 at room temperature (with an increment of 670% compared to that of VTE-BTS film). Consequently, the ZT value of the VTE@MS-BTS film at room temperature is estimated to be 1.0 (Fig. 4F), which is greater than that of other films prepared using MS and VTE methods alone (*18*, *21*, *25*, *51*, *53*, *65*–*67*).

Flexibility, heat harvesting, and cooling performance evaluation

In addition to the aforementioned ultrahigh electrical properties and ultralow thermal conductivity, the VTE@MS-BTS film also demonstrates exceptional deformation and strain absorption capabilities owing to SLs, AdLs, and nanopore structures coupled with enhanced orientation. The flexibility characterization (see Materials and Methods for details) suggests that our developed film could maintain 93% of initial electrical conductivity (σ/σ_0) even after 1000 bending cycles with a bending radius of $r = 5$ mm (Fig. 5A). This notable enhancement of flexibility surpasses that of MS- (76%) and VTE-BTS (85%) films and ensures a competitive bendability for device implementation. The resistance variations ($\Delta R/R_0$) for a unicouple prototype after 1000 bending cycles under various bending radii (5 to 9 mm) were below 10% (Fig. 5B). Moreover, according to the physical

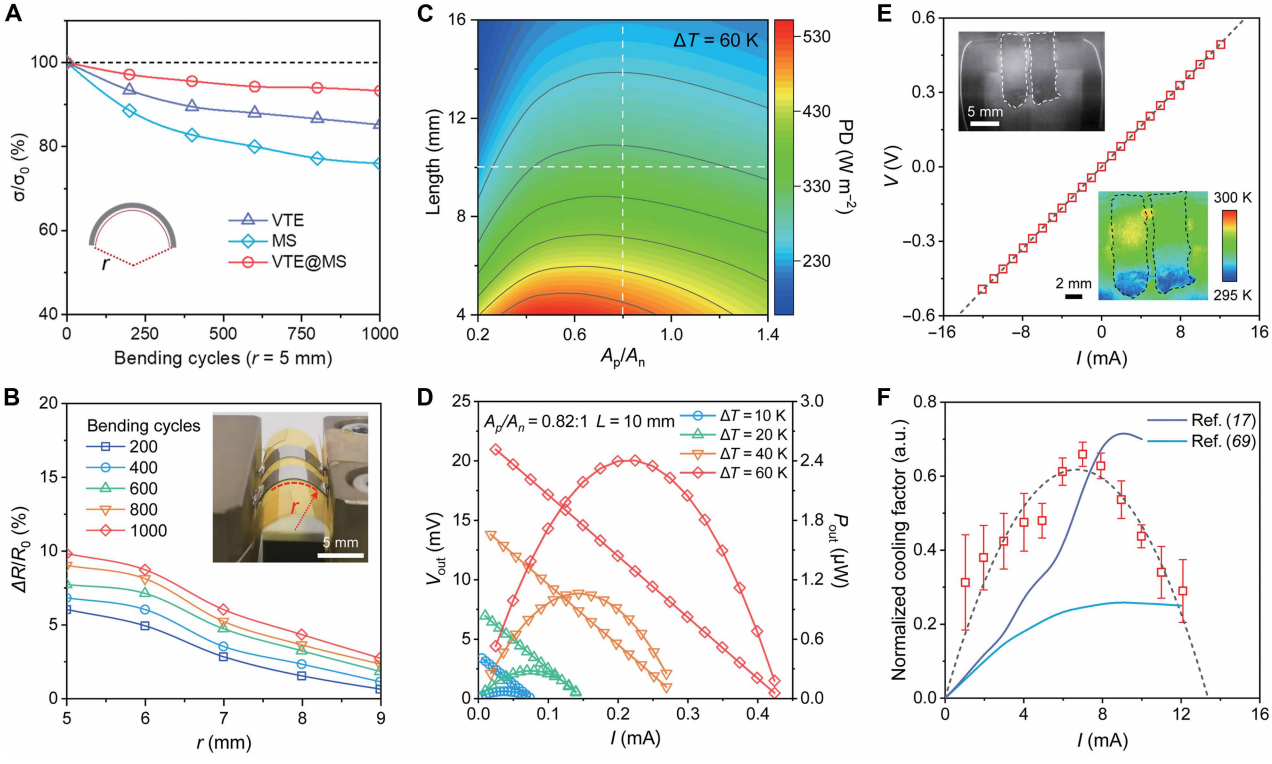

Fig. 5. Flexibility, heat harvesting, and cooling performance of thin-film devices. (**A**) σ/σ_0 under various bending cycles ($r = 5$ mm) for BTS thin films. (**B**) Resistance variation ($\Delta R/R_0$) of the minimally encapsulated prototype f-TEG under various bending cycles and bending radii. Inset: A prototype f-TEG with r of 7 mm. (**C**) Simulated maximum output power density (PD_{max}) versus geometry (A_p/A_n and length), $\Delta T = 60$ K. (**D**) Experimental output voltage (V_{out}) and power (P_{out}) as a function of electric current at various temperature differences. (**E**) Current (I)–voltage (V) characteristics of prototype TE cooler. Inset: The grayscale image of prototype TE cooler (top) and thermal image (bottom) of prototype TE cooler with an input current of 7 mA at 300 K. (**F**) Current dependence of normalized cooling factor of temperature drops for TE coolers to per-unit-area [$\Delta T/(N{\cdot}A_s)$, N represents the number of p-n leg pairs, and A_s is the area of the device]. Solid lines represent other film-based TE coolers reported in the literature.

design of device geometry [$A_p / A_n = \sqrt{(\kappa_n/\kappa_p)(\sigma_n/\sigma_p)}$], where the cross-sectional ratio (A_p / A_n) and length (L) of TE legs are pivotal in modulating thermal and electrical resistance toward the maximization of device ZT (*68*). Consequently, we performed finite-element simulation with variables A_p / A_n and L to determine the optimal geometry of TE legs for power density (PD, W m^{-2}) maximization (Fig. 5C; see Materials and Methods for details). We also evaluated the power output of fabricated devices according to modeling results by using a homemade platform (Fig. 5D and fig. S21; see Materials and Methods for details). The optimized unicouple ($A_p/A_n = 0.82$, $L = 10$ mm) achieved a maximum open-circuit voltage (V_{out}) of 22.0 mV and an output power (P_{out}) of 2.4 μW at $\Delta T = 60$ K, yielding a competitive PD_{max} of 300 W m^{-2}. The contact resistance (R_C) between the TE film and electrodes was characterized to be negligible (p-type film, 0.298 ohm; n-type film, 0.386 ohm; see fig. S22 and Materials and Methods for details) compared to the internal resistance (R_{in}, ~49 ohm; the *V-I* slope in Fig. 5D). In contrast, for devices configured with other geometries ($A_p/A_n = 1$, $L = 10$ mm; $A_p/A_n = 1$, $L = 20$ mm), a lower PD_{max} of 260 and 120 W m^{-2} achieved separately at the same conditions (fig. S23). We then calculated the normalized maximum power densities ($PD_{max}{\cdot}L/\Delta T^2$) of the proposed device, and the dimension- and temperature-independent variable $PD_{max}{\cdot}L/\Delta T^2$ of 0.84 mW m^{-1} K^{-2} is competitive with other results (fig. S24) (*17*, *20*, *25*, *28*–*38*). Furthermore, our unicouple TE cooler demonstrates good refrigeration performance, and a stable temperature drop of 0.8 K was obtained with a sole input current of 7 mA into the device (Fig. 5E and fig. S25). By normalizing the temperature drop to a per-unit area (Fig. 5F), our device is comparable to state-of-the-art film-based coolers in thermoelectrics (*17*, *69*). Besides that, the spatial uniformity of measured PF with a variation of <10% across a 120-cm^2 large area (fig. S26) ensures stable performance for scalable manufacturing and applications.

DISCUSSION

In summary, we explored a homo-layer flexible BTS thin film for sustainable low-grade heat harvesting and cooling. This innovative approach synergistically enhanced the Seebeck coefficient and electrical transport properties toward an ultrahigh power factor of 30.0 μW cm^{-1} K^{-2}. Meanwhile, the full-scale phonon scattering centers induced by homo-layer fusion process result in an exceptionally low lattice thermal conductivity of 0.38 W m^{-1} K^{-1}, yielding a high ZT value of 1.0 at room temperature. In addition, the fused texture film exhibited outstanding bendability, remaining 93% of its electrical conductivity after 1000 bending cycles with a 5-mm radius. These advancements led to a maximum output power density of 300 W m^{-2} at a 60 K temperature gradient and a normalized cooling factor of 0.6, sufficient for large-area production of up to 120 cm^2. Our industry-compatible and scalable homo-layer fusion deposition technique could provide a universal framework for structure-property relationship manipulation of inorganic TE thin films and advance solid-state electronic fabrication for sustainable heat harvesting and cooling applications.

MATERIALS AND METHODS

$Bi_2Te_{2.85}Se_{0.15}$ thin-film preparation

In this study, we used a hybrid approach combining MS and high-VTE techniques to fabricate n-type BTS thin films on PI substrates. A commercially available $Bi_2Te_{2.85}Se_{0.15}$ as the raw material, which was ground into fine powders, and then divided into two portions: One was formed into a circular target with a diameter of 2 inches (5.08 cm) through spark plasma sintering for subsequent MS deposition, while the other was shaped into compacted pellets with a weight of ~3.5 g for VTE deposition. Initially, an MS-BTS thin film with a thickness of 500 nm was deposited onto a clean PI substrate using the MS method. Without delay, this nascent bilayer film was transferred to the VTE apparatus, where an additional 500-nm-thick layer was deposited by modulating the current during the VTE process. Thus, a dual-processed VTE@MS-BTS thin film with a total thickness of 1 μm was obtained. The as-prepared film was then carefully enclosed in a quartz tube, maintaining a vacuum level of 3.0×10^{-4} Pa, and subjected to a rigorous annealing treatment ranging from 623 to 723 K for 2 hours. As a result of this annealing process, the interface between the two homo layers disappears, leading to the formation of a single homogenous film. For comparative analysis, MS-, VTE-, and VTE@*t*%MS-BTS films with a total thickness of 1 μm were deposited separately under consistent experimental conditions to ensure a fair basis for evaluating the impact of as-developed homo-layer annealing process.

Characterization and performance evaluation

The XRD results of all BTS thin films were obtained by a commercial instrument (Rigaku, Smartlab 9 kW) from 15° to 60°. The Copper radiation with $K_\alpha = 1.5418$ Å was equipped. The in-plane surface and cross-sectional microtopography of BTS thin films were studied by a scanning electron microscope (Zeiss Merlin, Germany) with an EDS probe. The surface layer on the thin films was removed by the Gatan PIPS II 695 equipment for analysis of nanopores in the films. The thickness of thin films was obtained by P-7 step profiler equipment manufactured by KLA Inc. Atomic structures of these samples were investigated by high-angle annular dark-field (HAADF) in STEM model on a double Cs-corrected TEM (Thermo Fisher Scientific Themis G2 60300) operated at 300 kV. The samples for STEM measurement were prepared using a FIB system, Helios 600i. The precision ion polishing system (PIPS; Gatan PIPS II 695) is used for plan-view thinning and polishing of the BTS films for EBSD analysis. The in-plane Seebeck coefficients and electrical conductivities of the BTS thin films were measured using ZEM-5 equipment manufactured by ULVAC-RIKO Inc. The n and μ of the BTS thin films were estimated by $n_H = 1/(eR_H)$ and $\mu_H = \sigma R_H$, and the Hall coefficient R_H was tested by PPMS equipment (physical property measurement system; Quantum Design, America). The total thermal conductivity (κ_{tot}) was calculated from the formula $\kappa_{tot} = \alpha_{TE}\rho C_p$, where the thermal diffusivity (α_{TE}) was measured using a TPET method, the geometrical density (ρ) was obtained by accurately weighing the mass before and after deposition on the PI substrate divided by the volume of the films, and the specific heat capacity (C_p) of BTS thin films was estimated using Dulong-Petit law. The systematic nanoindentation characterization was performed by using a Bruker Hysitron TI950 system (load range, 70 nN to 10 mN; load resolution, ≤1 nN; load displacement resolution, ≤0.006 nm; thermal drift, ≤0.05 nm s^{-1}) with BTS films before and after six transport experiment (TE) cycles.

Orientation factor calculation

The preferential orientations of the BTS films can be expressed by the orientation factor $F(X)$ corresponding to XRD patterns. According to Lotgering's method, the formula is as follows (*18*)

$$P_0 = \frac{\sum I_0(X)}{\sum I_0(hkl)} \quad (5)$$

$$P = \frac{\sum I(X)}{\sum I(hkl)} \quad (6)$$

$$F(X) = \frac{(P - P_0)}{(1 - P_0)} \quad (7)$$

where $\sum I_0(X)$, $\sum I(X)$, $\sum I_0(hkl)$, and $\sum I(hkl)$ are the sum of the integral intensity of the (X)-plane and all (hkl) planes of the randomly oriented sample captured from the PDF card and measured samples, respectively. P_0 and P are the ratios of the sums of the randomly oriented sample and the measured one. A closer value to 1 of $F(X)$ will indicate a stronger orientation at (X) plane.

SPB calculation

The relationship of S, μ_H, n_H, and L_0 can be described by the SPB model (*17*)

$$S = \pm \frac{k_B}{e}\left[\frac{\left(\lambda + \frac{5}{2}\right)F_{\lambda+\frac{3}{2}}(\eta)}{\left(\lambda + \frac{3}{2}\right)F_{\lambda+\frac{1}{2}}(\eta)} - \eta\right] \quad (8)$$

$$n_H = \frac{1}{eR_H} = \frac{(2m^* k_B T)^{\frac{3}{2}}}{3\pi^2\hbar^3}\left[\frac{\left(\lambda + \frac{3}{2}\right)^2 F_{\lambda+\frac{1}{2}}(\eta)}{\left(2\lambda + \frac{3}{2}\right)F_{2\lambda+\frac{1}{2}}(\eta)}\right] \quad (9)$$

$$\mu = \left[\frac{e\pi\hbar^4}{\sqrt{2}(k_8 T)^{\frac{3}{2}}}\frac{C_l}{E_{def}^2 (m^*)^{\frac{5}{2}}}\right]\frac{\left(2\lambda + \frac{3}{2}\right)F_{2\lambda+\frac{1}{2}}(\eta)}{\left(\lambda + \frac{3}{2}\right)^2 F_{\lambda+\frac{1}{2}}(\eta)} \quad (10)$$

$$L_0 = \left(\frac{k_B}{e}\right)^2\left\{\frac{\left(\lambda + \frac{7}{2}\right)F_{r+\frac{5}{2}}(\eta)}{\left(\lambda + \frac{3}{2}\right)F_{r+\frac{1}{2}}(\eta)} - \left[\frac{\left(\lambda + \frac{5}{2}\right)F_{r+\frac{3}{2}}(\eta)}{\left(\lambda + \frac{3}{2}\right)F_{r+\frac{1}{2}}(\eta)}\right]^2\right\} \quad (11)$$

$$F_n(\eta) = \int_0^\infty \frac{x^n}{1 + \exp(x - \eta)}dx \quad (12)$$

where λ is the carrier scattering parameter ($\lambda = -1/2$ for acoustic phonon scattering), e is the electron charge, R_H is the Hall coefficient, $F_n(\eta)$ is the Fermi integral, η is the reduced Fermi energy, E_{def} is the deformation potential coefficient, and C_l is the elastic constant for longitudinal vibrations ($C_l = \nu_l^2 \rho$, where ν_l is the longitudinal sound velocity and ρ is the mass density), respectively.

DFT calculation and finite element simulation

All DFT calculations were performed using the Vienna Ab initio Simulation Package (VASP) (*70*, *71*). The electronic exchange-correlation interactions were described by the generalized gradient approximation with the Perdew-Burke-Ernzerhof functional (*72*). Plane-wave cutoff energy convergence tests demonstrated that an energy cutoff of 400 eV achieved excellent convergence in total energy calculations. The convergence criteria for the electronic self-consistent field iterations and ionic relaxations were set to 1×10^{-6} eV and 0.01 eV/Å, respectively. For the Brillouin zone sampling, a Monkhorst-Pack k-point grid of $1 \times 6 \times 1$ was used during structural optimization, selected on the basis of the supercell dimensions and symmetry considerations. The vdW interactions were accounted for using the DFT-D3 dispersion correction method. The optimized lattice parameters of the Bi_2Te_3 unit cell ($a = 4.43$ Å, $c = 30.50$ Å) demonstrate excellent agreement with experimental values ($a = 4.39$ Å, $c = 30.50$ Å) measured at 300 K. Band structure calculations were performed using the VASPKIT postprocessing toolkit (*73*). A series of distinct structural models were constructed: (i) a regular orthogonal configuration with five quintuple layers (120 atoms), (ii) an AdL model (120 atoms), (iii) a defective orthogonal configuration featuring SL stacking (96 atoms), and (iv) five defect-controlled models (designated V_{Te}-1 to V_{Te}-5) with systematically increasing anion vacancy concentrations. These vacancy-controlled systems were constructed to $Bi_{48}Te_{71}$, $Bi_{48}Te_{70}$, $Bi_{48}Te_{69}$, $Bi_{48}Te_{68}$, and $Bi_{48}Te_{67}$, corresponding to 0.8, 1.6, 2.5, 3.3, and 4.2% anion vacancy concentrations, respectively. Atomic configurations were visualized using VESTA software.

Finite element analysis (FEA) was used to facilitate geometry-dependent optimization for the f-TEG. The geometry-dependent power output of Bi_2Te_3-based f-TEG was performed by using COMSOL Multiphysics coupled with Heat Transfer in Solids, Electric Currents, and Electrical Circuit modules. The Thermoelectric Effect and Electromagnetic Heating are included in Multiphysics, and detailed flowcharts and component definitions can be found in our previous work (*68*). The measured thermoelectric properties of VTE@MS BTS films in this work and p-type Bi_2Te_3 films previously reported (*27*) were used in the simulation. The hot- and cold-side temperatures were fixed at 370 and 310 K, respectively, according to the experimental thermal measurement. The length (L) of p- and n-type Bi_2Te_3-based films, as well as the cross-sectional area ratio (A_p/A_n) between p- and n-type legs, were parametrically swept to capture the optimum value of L versus A_p/A_n to determine the maximum power output. The maximal power density was estimated by using 0.25 times the open-circuit voltage and short-circuit current with respect to variable cross-sectional areas of p- and n-type legs.

Thermal conductivity measurement

A TPET technique was used to measure the thermal conductivity of BTS thin films with PI substrate. A TPET technique using laser beam heating can minimize the influence of the Peltier effect, thus improving the test accuracy (*27*, *74*). In a typical TPET measurement, as illustrated by the test schematic in fig. S19, the extracted α_{mea} includes the heat conduction (α_{con}), an effect of heat dissipation

through convection (α_{cov}) and thermal radiation (α_{rad}), as expressed in the following equation (*74*, *75*)

$$\alpha_{mea.} = \alpha_{con.} + \alpha_{cov.} + \alpha_{rad.} = \alpha_{con.} + \frac{1}{\rho c_p}\left(\frac{2h}{\pi^2} + \frac{8\xi\sigma T^3}{\pi^2}\right)\frac{L^2}{d} \quad (13)$$

where α_{con} is the real thermal diffusivity of the sample; ρ, c_p, σ, ξ, d, and L are the mass density, specific heat, Stefan-Boltzmann constant, emissivity, thickness, and length of the sample, respectively. The α_{con} of the double-layered sample can be obtained by measuring samples with different lengths and linear fitting of α_{mea} versus L^2, and the raw data for all temperature points have been provided in fig. S20. Furthermore, the real thermal diffusivity of the BTS film (α_{TE}) can be calculated as below

$$\alpha_{con} = C_1\alpha_{TE} + C_2\alpha_{sub} \quad (14)$$

$$C_1 = \frac{\rho_{TE}C_{TE}d_{TE}}{\rho_{TE}C_{TE}d_{TE} + \rho_{sub}C_{sub}d_{sub}} \quad (15)$$

$$C_2 = \frac{\rho_{sub}C_{sub}d_{sub}}{\rho_{TE}C_{TE}d_{TE} + \rho_{sub}C_{sub}d_{sub}} \quad (16)$$

where ρ_{sub} and d_{sub} of PI substrate are 1390 kg m^{-3} and 5 μm, respectively. Last, the thermal conductivity of BTS films can be calculated by $\kappa_{tot} = \rho c_p \alpha_{TE}$, where c_p used in the calculation is 159 J kg^{-1} K^{-1} for BTS films. The measurement uncertainty for TE films using the TPET technique can be reduced to below 10%.

Debye-Callaway model calculation

According to the classical Debye-Callaway model (*54*, *57*–*60*), the lattice thermal conductivity κ_l associated with the different phonon scattering mechanisms can be expressed as

$$\kappa_l = \frac{k_B}{2\pi^2 v_a}\left(\frac{k_B T}{\hbar}\right)^3 \int_0^{\frac{\theta_D}{T}} \frac{x^4 e^x}{\tau_C^{-1}(e^x-1)^2}dx \quad (17)$$

where k_B, $\hbar$, v_a, and θ_D are the Boltzmann constant, reduced Planck constant, average sound velocity, and Debye temperature, respectively. $x = \hbar\omega / k_B T$ is the simplified phonon frequency, and ω is the phonon frequency. The overall phonon scattering relaxation time is expressed as

$$\tau_C^{-1} = \tau_U^{-1} + \tau_{GB}^{-1} + \tau_{PD}^{-1} + \tau_D^{-1} + \tau_{SF}^{-1} \quad (18)$$

Umklapp scattering (U) occurs when phonons within a crystal scatter off other phonons, and the relaxation time for this process follows a specific formula

$$\tau_U^{-1} = A_N \frac{h\gamma^2}{M v_s^2 \theta_D}\omega^2 T \exp\left(-\frac{\theta_D}{3T}\right) \quad (19)$$

where γ and M are the Grüneisen parameter and the atomic mass. The relaxation time for the Normal process is considered as an additional factor, represented by A_N.

For common grain boundaries scattering (GB), the frequency-independent τ_{GB}^{-1} is given by

$$\tau_{GB}^{-1} = \frac{\nu}{d} \quad (20)$$

where d is the experimentally determined grain size.

The relaxation time of point defect scattering (PD) is calculated by

$$\tau_{PD}^{-1} = \frac{V\omega^4}{4\pi v_s^3}\Gamma \quad (21)$$

where V is the average atom volume, and Γ is the disorder parameter of mass field fluctuations (Γ_M) and strain field fluctuations (Γ_S).

The dislocation scattering (D) can be treated as two parts: dislocation cores and dislocation strain. The relaxation time with this process is represented in the equation

$$\tau_D^{-1} = N_D\frac{V^{4/3}}{v^2}\omega^3 + 0.6B_D^2 N_D(\gamma+\Delta\gamma)^2 \left\{\frac{1}{2} + \frac{1}{24}\left(\frac{1-2r}{1-r}\right)^2\left[1+\sqrt{2}\left(\frac{v_l}{v_t}\right)\right]^2\right\}\omega \quad (22)$$

where N_D, B_D, $\Delta\gamma$, v_l, v_t, and r are the dislocation density, effective Burger's vector, change in Grüneisen parameter due to the dislocation strain, longitudinal sound velocity, transverse sound velocity, and Poisson's ratio, respectively.

For SL and AdL scattering (SF), we adopt an approximate calculation method from the stacking faults theoretical model here (*69*, *76*, *77*)

$$\tau_{SF}^{-1} = 0.7N_s\frac{a^2}{v}\gamma^2\omega^2 \quad (23)$$

where a is the lattice parameter, and N_s is the density of SLs. All the calculated parameters can be found in table S5.

Device fabrication and characterization

The π-shape unicouple device consists of a VTE@MS BTS strip (from this work), and a p-type $Bi_{0.4}Sb_{1.6}Te_3$ strip (from our previous work) (*27*) was assembled on a PI substrate. The electrical connection was made in series, while the thermal path was connected in parallel, using indium welding and Pt-Rh wires for bonding. The p- and n-type legs feature 10-mm length with 5-mm interleg spacing, maintaining a 0.82 cross-sectional area ratio (A_p/A_n, guided by FEA optimization in Fig. 5C) that enables a compact 15 mm by 15 mm f-TEG configuration. Moreover, the flexibility was assessed by measuring resistance variations ($\Delta R/R_0$) using a custom-built tensile tester at a speed of 5 mm s^{-1}. A home-made testing system was established to evaluate the electrical power density of the f-TEG device. During the test, a Keithley 2400 source meter was used as an ammeter, and a Keithley 2182A meter was used as a voltmeter. In terms of the TE cooling measurement, the fabrication of unicouple device is consistent with that of the above f-TEG, and the adjacent distance between p- and n-type legs is 1 mm. A lock-in thermal microscopy (NT100 from Microsanj LLC, USA) was used to evaluate the temperature drop of an as-fabricated unicouple cooler under variable input currents. The temperature measurement error is ~4%. Moreover, the electrical contact resistances (R_C) of TE film-to-electrode interface were measured by using the transmission line method according to previous works (*6*, *68*), as illustrated in fig. S22.

Supplementary Materials

This PDF file includes:

Figs. S1 to S26

Tables S1 to S5

REFERENCES AND NOTES

1. W. Chen, X.-L. Shi, M. Li, T. Liu, Y. Mao, Q. Liu, M. Dargusch, J. Zou, G. Q. Lu, Z.-G. Chen, Nanobinders advance screen-printed flexible thermoelectrics. *Science* **386**, 1265–1271 (2024).
2. B. Jia, D. Wu, L. Xie, W. Wang, T. Yu, S. Li, Y. Wang, Y. Xu, B. Jiang, Z. Chen, Y. Weng, J. He, Pseudo-nanostructure and trapped-hole release induce high thermoelectric performance in PbTe. *Science* **384**, 81–86 (2024).
3. B. Qin, D. Wang, X. Liu, Y. Qin, J.-F. Dong, J. Luo, J.-W. Li, W. Liu, G. Tan, X. Tang, J.-F. Li, J. He, L.-D. Zhao, Power generation and thermoelectric cooling enabled by momentum and energy multiband alignments. *Science* **373**, 556–561 (2021).
4. M. Wei, X.-L. Shi, Z.-H. Zheng, F. Li, W.-D. Liu, L.-P. Xiang, Y.-S. Xie, Y.-X. Chen, J.-Y. Duan, H.-L. Ma, G.-X. Liang, X.-H. Zhang, P. Fan, Z.-G. Chen, Directional thermal diffusion realizing inorganic Sb_2Te_3/Te hybrid thin films with high thermoelectric performance and flexibility. *Adv. Funct. Mater.* **32**, 2207903 (2022).
5. Q. Jin, Y. Zhao, X. Long, S. Jiang, C. Qian, F. Ding, Z. Wang, X. Li, Z. Yu, J. He, Y. Song, H. Yu, Y. Wan, K. Tai, N. Gao, J. Tan, C. Liu, H.-M. Cheng, Flexible carbon nanotube-epitaxially grown nanocrystals for micro-thermoelectric modules. *Adv. Mater.* **35**, e2304751 (2023).
6. Y. Lu, Y. Zhou, W. Wang, M. Hu, X. Huang, D. Mao, S. Huang, L. Xie, P. Lin, B. Jiang, B. Zhu, J. Feng, J. Shi, Q. Lou, Y. Huang, J. Yang, J. Li, G. Li, J. He, Staggered-layer-boosted flexible Bi_2Te_3 films with high thermoelectric performance. *Nat. Nanotechnol.* **18**, 1281–1288 (2023).
7. T. Deng, Z. Gao, Z. Li, P. Qiu, Z. Li, X. Yuan, C. Ming, T.-R. Wei, L. Chen, X. Shi, Room-temperature exceptional plasticity in defective Bi_2Te_3-based bulk thermoelectric crystals. *Science* **386**, 1112–1117 (2024).
8. Q. Yang, S. Yang, P. Qiu, L. Peng, T.-R. Wei, Z. Zhang, X. Shi, L. Chen, Flexible thermoelectrics based on ductile semiconductors. *Science* **377**, 854–858 (2022).
9. X. Tang, Z. Li, W. Liu, Q. Zhang, C. Uher, A comprehensive review on Bi_2Te_3-based thin films: Thermoelectrics and beyond. *Interdiscip. Mater.* **1**, 88–115 (2022).
10. X. Chen, Z. Zhou, Y.-H. Lin, C. Nan, Thermoelectric thin films: Promising strategies and related mechanism on boosting energy conversion performance. *J. Materiomics* **6**, 494–512 (2020).
11. B. Hu, X.-L. Shi, T. Cao, M. Li, W. Chen, W.-D. Liu, W. Lyu, T. Tesfamichael, Z.-G. Chen, Advances in flexible thermoelectric materials and devices fabricated by magnetron sputtering. *Small Sci.* **5**, 2300061 (2025).
12. Z. Liang, R. Shu, C. Xu, Y. Wang, H. Shang, J. Mao, Z. Ren, Substrate-free inorganic-based films for thermoelectric applications. *Adv. Mater.* **37**, e2416394 (2025).
13. T. Cao, X.-L. Shi, M. Li, B. Hu, W. Chen, W.-D. Liu, W. Lyu, J. MacLeod, Z.-G. Chen, Advances in bismuth-telluride-based thermoelectric devices: Progress and challenges. *eScience* **3**, 100122 (2023).
14. J. Pei, B. Cai, H.-L. Zhuang, J.-F. Li, Bi_2Te_3-based applied thermoelectric materials: Research advances and new challenges. *Natl. Sci. Rev.* **7**, 1856–1858 (2020).
15. I. T. Witting, T. C. Chasapis, F. Ricci, M. Peters, N. A. Heinz, G. Hautier, G. J. Snyder, The thermoelectric properties of bismuth telluride. *Adv. Electron. Mater.* **5**, 1800904 (2019).
16. B. Zhu, X. Liu, Q. Wang, Y. Qiu, Z. Shu, Z. Guo, Y. Tong, J. Cui, M. Gu, J. He, Realizing record high performance in n-type Bi_2Te_3-based thermoelectric materials. *Energ. Environ. Sci.* **13**, 2106–2114 (2020).
17. Z.-H. Zheng, X.-L. Shi, D.-W. Ao, W.-D. Liu, M. Li, L.-Z. Kou, Y.-X. Chen, F. Li, M. Wei, G.-X. Liang, P. Fan, G. Q. Lu, Z.-G. Chen, Harvesting waste heat with flexible Bi_2Te_3 thermoelectric thin film. *Nat. Sustain.* **6**, 180–191 (2023).
18. Q. Jin, S. Jiang, Y. Zhao, D. Wang, J. Qiu, D.-M. Tang, J. Tan, D.-M. Sun, P.-X. Hou, X.-Q. Chen, K. Tai, N. Gao, C. Liu, H.-M. Cheng, X. Jiang, Flexible layer-structured Bi_2Te_3 thermoelectric on a carbon nanotube scaffold. *Nat. Mater.* **18**, 62–68 (2019).
19. H.-J. Shang, F.-Z. Ding, Y. Deng, H. Zhang, Z.-B. Dong, W.-J. Xu, D.-X. Huang, H.-W. Gu, Z.-G. Chen, Highly (00l)-oriented Bi_2Te_3/Te heterostructure thin films with enhanced power factor. *Nanoscale* **10**, 20189–20195 (2018).
20. D.-W. Ao, W.-D. Liu, Z.-H. Zheng, X.-L. Shi, M. Wei, Y.-M. Zhong, M. Li, G.-X. Liang, P. Fan, Z.-G. Chen, Assembly-free fabrication of high-performance flexible inorganic thin-film thermoelectric device prepared by a thermal diffusion. *Adv. Energy Mater.* **12**, 2202731 (2022).
21. Z.-H. Zheng, D. Yang, P.-C. Zhang, F. Li, Y.-X. Chen, G.-X. Liang, P. Fan, Enhancement of the thermoelectric properties of Bi_2Te_3 nanocrystal thin films by rapid annealing. *Mater. Lett.* **275**, 128143 (2020).
22. A. M. Adam, E. Lilov, P. Petkov, Optical and thermoelectric properties of nano-particles based $Bi_2(Te_{1-x}Se_x)_3$ thin films. *Superlattices Microstruct.* **101**, 609–624 (2017).
23. J.-M. Lin, Y.-C. Chen, C.-P. Lin, Annealing effect on the thermoelectric properties of Bi_2Te_3 thin films prepared by thermal evaporation method. *J. Nanomater.* **2013**, 201017 (2013).
24. J.-H. Kim, J.-Y. Choi, J.-M. Bae, M. Kim, T. S. J. M. T. Oh, Thermoelectric characteristics of n-type Bi_2Te_3 and p-type Sb_2Te_3 thin films prepared by co-evaporation and annealing for thermopile sensor applications. *Mater. Trans.* **54**, 618–625 (2013).
25. Y. Tian, I. Florenciano, H. Xia, Q. Li, H. E. Baysal, D. Zhu, E. Ramunni, S. Meyers, T.-Y. Yu, K. Baert, T. Hauffman, S. Nider, B. Göksel, F. Molina-Lopez, Facile fabrication of flexible and high-performing thermoelectrics by direct laser printing on plastic foil. *Adv. Mater.* **36**, 2307945 (2024).
26. B. Wu, Y. Guo, C. Hou, Q. Zhang, Y. Li, H. Wang, High-performance flexible thermoelectric devices based on all-inorganic hybrid films for harvesting low-grade heat. *Adv. Funct. Mater.* **29**, 1900304 (2019).
27. D. Mao, Y. Zhou, Y. Yu, Y. Wang, M. Han, Q. Meng, Y. Lu, J. Feng, M. Kong, H. Yang, Q. Gan, X. Xu, L. Xie, G. W. Ho, J. He, Scalable and sustainable manufacturing of twin boundary-enhanced flexible $Bi_{0.4}Sb_{1.6}Te_3$ films with high thermoelectric performance. *Joule* **8**, 3313–3323 (2024).
28. D. Yang, X.-L. Shi, M. Li, M. Nisar, A. Mansoor, S. Chen, Y. Chen, F. Li, H. Ma, G. X. Liang, X. Zhang, W. Liu, P. Fan, Z. Zheng, Z.-G. Chen, Flexible power generators by Ag_2Se thin films with record-high thermoelectric performance. *Nat. Commun.* **15**, 923 (2024).
29. J. Liang, T. Wang, P. Qiu, S. Yang, C. Ming, H. Chen, Q. Song, K. Zhao, T.-R. Wei, D. Ren, Y.-Y. Sun, X. Shi, J. He, L. Chen, Flexible thermoelectrics: From silver chalcogenides to full-inorganic devices. *Energ. Environ. Sci.* **12**, 2983–2990 (2019).
30. Y. Liu, Q. Zhang, A. Huang, K. Zhang, S. Wan, H. Chen, Y. Fu, W. Zuo, Y. Wang, X. Cao, L. Wang, U. Lemmer, W. Jiang, Fully inkjet-printed Ag_2Se flexible thermoelectric devices for sustainable power generation. *Nat. Commun.* **15**, 2141 (2024).
31. Y. Ding, Y. Qiu, K. Cai, Q. Yao, S. Chen, L. Chen, J. He, High performance n-type Ag_2Se film on nylon membrane for flexible thermoelectric power generator. *Nat. Commun.* **10**, 841 (2019).
32. Z. Guo, Y. Yu, W. Zhu, Q. Zhang, Y. Liu, J. Zhou, Y. Wang, J. Xing, Y. Deng, Kirigami-based stretchable, deformable, ultralight thin-film thermoelectric generator for bodyNET application. *Adv. Energy Mater.* **12**, 2102993 (2022).
33. D. Yang, D. Zhang, D. Ao, M. Nisar, A. Mansoor, Y. Chen, F. Li, H. Ma, G. Liang, X. Zhang, P. Fan, Z. Zheng, High thermoelectric performance of aluminum-doped cuprous selenide thin films with exceptional flexibility for wearable applications. *Nano Energy* **117**, 108930 (2023).
34. C. Yang, D. Souchay, M. Kneiß, M. Bogner, H. M. Wei, M. Lorenz, O. Oeckler, G. Benstetter, Y. Q. Fu, M. Grundmann, Transparent flexible thermoelectric material based on non-toxic earth-abundant p-type copper iodide thin film. *Nat. Commun.* **8**, 16076 (2017).
35. T. Deng, Z. Gao, P. Qiu, Z. Zhou, C. Ming, Z. Liu, Z. Li, S. Yang, T.-R. Wei, G. Wang, L. Chen, X. Shi, High thermoelectric power factors in plastic/ductile bulk $SnSe_2$-based crystals. *Adv. Mater.* **36**, e2304219 (2024).
36. Y. Xue, Q. Wang, Z. Gao, X. Qian, J. Wang, G. Yan, M. Chen, L.-D. Zhao, S.-F. Wang, Z. Li, Constructing quasi-layered and self-hole doped SnSe oriented films to achieve excellent thermoelectric power factor and output power density. *Sci. Bull.* **68**, 2769–2778 (2023).
37. D. Li, X.-L. Shi, J. Zhu, T. Cao, X. Ma, M. Li, Z. Han, Z. Feng, Y. Chen, J. Wang, W.-D. Liu, H. Zhong, S. Li, Z.-G. Chen, High-performance flexible p-type Ce-filled Fe_3CoSb_{12} skutterudite thin film for medium-to-high-temperature applications. *Nat. Commun.* **15**, 4242 (2024).
38. L. Wang, Z. Zhang, L. Geng, T. Yuan, Y. Liu, J. Guo, L. Fang, J. Qiu, S. Wang, Solution-printable fullerene/TiS_2 organic/inorganic hybrids for high-performance flexible n-type thermoelectrics. *Energ. Environ. Sci.* **11**, 1307–1317 (2018).
39. C. Jiang, P. Wei, Y. Ding, K. Cai, L. Tong, Q. Gao, Y. Lu, W. Zhao, S. Chen, Ultrahigh performance polyvinylpyrrolidone/Ag_2Se composite thermoelectric film for flexible energy harvesting. *Nano Energy* **80**, 105488 (2021).
40. J. Jung, E. H. Suh, Y. J. Jeong, H. S. Yang, T. Lee, J. Jang, Efficient debundling of few-walled carbon nanotubes by wrapping with donor–acceptor polymers for improving thermoelectric properties. *ACS Appl. Mater. Interfaces* **11**, 47330–47339 (2019).
41. Q. Xu, S. Qu, C. Ming, P. Qiu, Q. Yao, C. Zhu, T.-R. Wei, J. He, X. Shi, L. Chen, Conformal organic–inorganic semiconductor composites for flexible thermoelectrics. *Energ. Environ. Sci.* **13**, 511–518 (2020).
42. L. Yang, S. Jiang, Y. Chen, C. Li, Z. Xu, Q. Ni, Effect of multi-scale film interfaces on CFEP composite mechanical properties based on magnetron sputtering technology. *Diamond Relat. Mater.* **139**, 110355 (2023).
43. J. Qiao, Y. Zhao, Q. Jin, J. Tan, S. Kang, J. Qiu, K. Tai, Tailoring nanoporous structures in Bi_2Te_3 thin films for improved thermoelectric performance. *ACS Appl. Mater. Interfaces* **11**, 38075–38083 (2019).
44. V. Senthil Velan, G. Velayutham, N. Rajalakshmi, K. S. Dhathathreyan, Influence of compressive stress on the pore structure of carbon cloth based gas diffusion layer investigated by capillary flow porometry. *Int. J. Hydrogen Energy* **39**, 1752–1759 (2014).
45. M. Huff, Review paper: Residual stresses in deposited thin-film material layers for micro- and nano-systems manufacturing. *Micromachines* **13**, 2084 (2022).
46. Z. Wu, E. Mu, Z. Che, Y. Liu, F. Sun, X. Wang, Z. Hu, Nanoporous (*00l*)-oriented Bi_2Te_3 nanoplate film for improved thermoelectric performance. *J. Alloys Compd.* **828**, 154239 (2020).
47. Y. Li, S. Bai, Y. Wen, Z. Zhao, L. Wang, S. Liu, J. Zheng, S. Wang, S. Liu, D. Gao, D. Liu, Y. Zhu, Q. Cao, X. Gao, H. Xie, L.-D. Zhao, Realizing high-efficiency thermoelectric module by suppressing donor-like effect and improving preferred orientation in n-type $Bi_2(Te, Se)_3$. *Sci. Bull.* **69**, 1728–1737 (2024).
48. L. Hu, H. Wu, T. Zhu, C. Fu, J. He, P. Ying, X. Zhao, Tuning multiscale microstructures to enhance thermoelectric performance of n-type bismuth-telluride-based solid solutions. *Adv. Energy Mater.* **5**, 1500411 (2015).

49. T. Zhu, L. Hu, X. Zhao, J. He, New insights into intrinsic point defects in V_2VI_3 thermoelectric materials. *Adv. Sci.* **3**, 1600004 (2016).
50. Y. Pan, T.-R. Wei, C.-F. Wu, J.-F. Li, Electrical and thermal transport properties of spark plasma sintered n-type $Bi_2Te_{3-x}Se_x$ alloys: The combined effect of point defect and Se content. *J. Mater. Chem. C* **3**, 10583–10589 (2015).
51. Z. Li, X. Yang, Z. Gao, J. Wang, Y. Xue, J. Wang, Q. Cao, Z. Ding, S. Wang, Remarkable average thermoelectric performance of the highly oriented Bi(Te, Se)-based thin films and devices. *J. Materiomics* **10**, 366–376 (2024).
52. D.-W. Ao, W.-D. Liu, Y.-X. Chen, M. Wei, B. Jabar, F. Li, X.-L. Shi, Z.-H. Zheng, G.-X. Liang, X.-H. Zhang, P. Fan, Z.-G. Chen, Novel thermal diffusion temperature engineering leading to high thermoelectric performance in Bi_2Te_3-based flexible thin-films. *Adv. Sci.* **9**, 2103547 (2022).
53. Y. Zhao, Y. Li, J. Qiao, S. Jiang, P. Mao, J. Qiu, S. Kang, J. Tan, K. Tai, C. Liu, Decoupling phonon and carrier scattering at carbon nanotube/Bi_2Te_3 interfaces for improved thermoelectric performance. *Carbon* **170**, 191–198 (2020).
54. G. Wu, Q. Zhang, X. Tan, Y. Fu, Z. Guo, Z. Zhang, Q. Sun, Y. Liu, H. Shi, J. Li, J. G. Noudem, J. Wu, G.-Q. Liu, P. Sun, H. Hu, J. Jiang, Bi_2Te_3-based thermoelectric modules for efficient and reliable low-grade heat recovery. *Adv. Mater.* **36**, e2400285 (2024).
55. G. J. Snyder, E. S. Toberer, Complex thermoelectric materials. *Nat. Mater.* **7**, 105–114 (2008).
56. Y. Yu, D.-S. He, S. Zhang, O. Cojocaru-Mirédin, T. Schwarz, A. Stoffers, X.-Y. Wang, S. Zheng, B. Zhu, C. Scheu, D. Wu, J.-Q. He, M. Wuttig, Z.-Y. Huang, F.-Q. Zu, Simultaneous optimization of electrical and thermal transport properties of $Bi_{0.5}Sb_{1.5}Te_3$ thermoelectric alloy by twin boundary engineering. *Nano Energy* **37**, 203–213 (2017).
57. X. Xu, J. Cui, Y. Yu, B. Zhu, Y. Huang, L. Xie, D. Wu, J. He, Constructing van der Waals gaps in cubic-structured SnTe-based thermoelectric materials. *Energ. Environ. Sci.* **13**, 5135–5142 (2020).
58. L. Fu, M. Yin, D. Wu, W. Li, D. Feng, L. Huang, J. He, Large enhancement of thermoelectric properties in n-type PbTe via dual-site point defects. *Energ. Environ. Sci.* **10**, 2030–2040 (2017).
59. Q. Zhang, Y. Lin, N. Lin, Y. Yu, F. Liu, C. Fu, B. Ge, O. Cojocaru-Mirédin, T. Zhu, X. Zhao, Enhancing the room temperature thermoelectric performance of n-type Bismuth-telluride-based polycrystalline materials by low-angle grain boundaries. *Mater. Today Phys.* **22**, 100573 (2022).
60. Y.-K. Zhu, Y. Sun, X. Dong, L. Yin, M. Liu, M. Guo, H. Wu, F. Li, Z. Guo, X. Wang, K. Yu, F. Guo, Q. Zhang, Z. Liu, W. Cai, J. Sui, General design of high-performance and textured layered thermoelectric materials via stacking of mechanically exfoliated crystals. *Joule* **8**, 2412–2424 (2024).
61. Y. Wang, L. Xie, H. Yang, M. Hu, X. Qian, R. Yang, J. He, Strong orbital-lattice coupling induces glassy thermal conductivity in high-symmetry single crystal $BaTiS_3$. *Phys. Rev. X* **15**, 011066 (2025).
62. M. U. Muzaffar, B. Zhu, Q. Yang, Y. Zhou, S. Zhang, Z. Zhang, J. He, Suppressing bipolar effect to broadening the optimum range of thermoelectric performance for p-type bismuth telluride–based alloys via calcium doping. *Mater. Today Phys.* **9**, 100130 (2019).
63. J. He, T. M. Tritt, Advances in thermoelectric materials research: Looking back and moving forward. *Science* **357**, eaak9997 (2017).
64. G. J. Snyder, A. H. Snyder, M. Wood, R. Gurunathan, B. H. Snyder, C. Niu, Weighted mobility. *Adv. Mater.* **32**, 2001537 (2020).
65. Y. Li, J. Qiao, Y. Zhao, Q. Lan, P. Mao, J. Qiu, K. Tai, C. Liu, H. Cheng, A flexible thermoelectric device based on a Bi_2Te_3-carbon nanotube hybrid. *J. Mater. Sci. Technol.* **58**, 80–85 (2020).
66. X. Sun, Y. Yan, M. Kang, W. Zhao, K. Yan, H. Wang, R. Li, S. Zhao, X. Hua, B. Wang, W. Zhang, Y. Deng, General strategy for developing thick-film micro-thermoelectric coolers from material fabrication to device integration. *Nat. Commun.* **15**, 3870 (2024).
67. K. Liu, X. Tang, Y. Liu, Z. Xu, Z. Yuan, Z. Zhang, Enhancing the performance of fully-scaled structure-adjustable 3D thermoelectric devices based on cold–press sintering and molding. *Energy* **206**, 118096 (2020).
68. Y. Zhou, X. Liu, B. Jia, T. Ding, D. Mao, T. Wang, G. W. Ho, J. He, Physics-guided co-designing flexible thermoelectrics with techno-economic sustainability for low-grade heat harvesting. *Sci. Adv.* **9**, eadf5701 (2023).
69. G. Dong, J. Feng, G. Qiu, Y. Yang, Q. Chen, Y. Xiong, H. Wu, Y. Ling, L. Xi, C. Long, J. Lu, Y. Qiao, G. Li, J. Li, R. Liu, R. Sun, Oriented Bi_2Te_3-based films enabled high performance planar thermoelectric cooling device for hot spot elimination. *Nat. Commun.* **15**, 9695 (2024).
70. P. Hohenberg, W. Kohn, Inhomogeneous electron gas. *Phys. Rev.* **136**, B864–B871 (1964).
71. W. Kohn, L. J. Sham, Self-consistent equations including exchange and correlation effects. *Phys. Rev.* **140**, A1133–A1138 (1965).
72. J. P. Perdew, K. Burke, M. Ernzerhof, Generalized gradient approximation made simple. *Phys. Rev. Lett.* **77**, 3865–3868 (1996).
73. V. Wang, N. Xu, J.-C. Liu, G. Tang, W.-T. Geng, VASPKIT: A user-friendly interface facilitating high-throughput computing and analysis using VASP code. *Comput. Phys. Commun.* **267**, 108033 (2021).
74. Y. Ling, M. Han, J. Xie, G. Qiu, G. Dong, E. Min, P. Zhang, X. Zeng, R. Liu, R. Sun, Thermal conductivity measurement of thermoelectric films using transient Photo-Electro-Thermal technique. *Measurement* **217**, 113058 (2023).
75. T. Wang, X. Wang, J. Guo, Z. Luo, K. Cen, Characterization of thermal diffusivity of micro/nanoscale wires by transient photo-electro-thermal technique. *Appl. Phys. A* **87**, 599–605 (2007).
76. J. He, S. N. Girard, J.-C. Zheng, L. Zhao, M. G. Kanatzidis, V. P. Dravid, Strong phonon scattering by layer structured $PbSnS_2$ in PbTe based thermoelectric materials. *Adv. Mater.* **24**, 4440–4444 (2012).
77. B. K. Singh, V. J. Menon, K. C. Sood, Phonon conductivity of plastically deformed crystals: Role of stacking faults and dislocations. *Phys. Rev. B* **74**, 184302 (2006).

Acknowledgments

Funding: This research was supported by the National Key Research and Development Program of China (grant no. 2024YFA1210400), the National Natural Science Foundation of China (grant nos. 12434001 and 52461160258), Guangdong Provincial Key Laboratory of Advanced Thermoelectric Materials and Device Physics (grant no. 2024B1212010001), and the Outstanding Talents Training Fund in Shenzhen (grant no. 202108). Y.Z. and G.W.H. acknowledge support from Ministry of Education, Singapore (A-8000107-01-00). We also acknowledge the SEM and TEM resources from the Core Research Facilities at Southern University of Science and Technology. **Author contributions:** D.M., Y.Z., and J.H. conceived the general idea and designed the experiments. J.H. and G.W.H. supervised the project. D.M. fabricated the samples, characterized their performances and microstructures, and wrote the manuscript. Y.Z. contributed to the device modeling, fabrication, and characterization. J.Y. performed the TEM section. M.H. measured thermal conductivities. X.H. and G.L. performed the DFT calculations. B.J., Z.W., J.W., X.X., and L.X. contributed ideas for materials synthesis and characterization. All authors revised the manuscript. **Competing interests:** The authors declare that they have no competing interests. **Data and materials availability:** All data needed to evaluate the conclusions in the paper are present in the paper and/or the Supplementary Materials.

Submitted 18 May 2025
Accepted 5 August 2025
Published 5 September 2025
10.1126/sciadv.adz1019